Supplementary Information for: GaInP/GaAs three-terminal heterojunction bipolar transistor solar cell

Marius H. Zehender †, Simon A. Svatek †#, Myles A. Steiner ‡, Iván García †, Pablo García-Linares †, Emily L. Warren ‡, Adele C. Tamboli ‡, Antonio Martí †, Elisa Antolín *†

† Universidad Politécnica de Madrid – Instituto de Energía Solar, Avenida Complutense 30, 28040 Madrid, Spain

Universidad Politécnica de Madrid – Departamento de Sistemas Informáticos, C/ Alan Turing s/n, 28031 Madrid, Spain

‡ National Renewable Energy Laboratory (NREL), Golden, CO, 80401, USA

* Corresponding author: elisa.antolin@upm.es

This PDF file includes:

S1: Complete layer structure and doping profiling (SIMS)

S2: Supplementary band diagrams

S3: Device geometry and efficiency calculations

S4: Supplementary EQE data

S5: Modelling of optical absorption

S6: Supplementary characterization of luminescent coupling

S7: Dark *J-V* curves

S8: SIMS profile of compensated contact

S9: Series resistance model

S10: Voltage maps of the test device

S11: 2T HBTSC-on-Si architecture

S12: Top interdigitated and bottom interdigitated base contact

S1: Complete layer structure and doping profiling (SIMS)

a

Layer	Thickness [nm]	Material	N [cm^{-3}]
Contact	275	GaAs:Se	$4 \cdot 10^{19}$
Window	25	AlInP:Se	$1 \cdot 10^{19}$
Emitter	485	GaInP:Si	$4 \cdot 10^{17}$
Base	565	GaInP:Zn	$6 \cdot 10^{18}$
Collector	3000	GaAs:Si	$5 \cdot 10^{17}$
BSF	300	GaInP:Si	$1 \cdot 10^{18}$

b

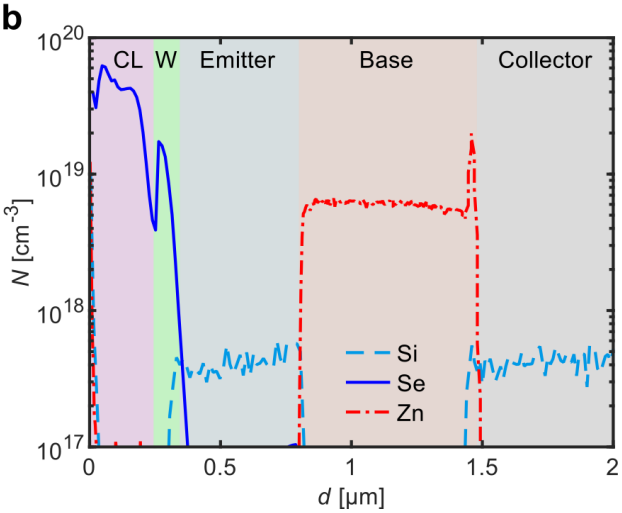

Figure S1: (a) Detailed layer structure of the HBTSC prototype, including layer thicknesses and concentration of dopant atoms (N) extracted from secondary ion mass spectroscopy (SIMS) profiles (performed by Loughborough Surface Analysis Ltd, UK). The layer thicknesses have been obtained from the modelling of the sample reflectance measured in-situ during growth (base and collector), from the fitting of the Fabry-Perot interferences in the EQE in Figure S6 (emitter) and from stylus profiling (contact layer). The thicknesses of window and BSF layers are nominal. (b) SIMS profile of N as a function of depth (d) of an epitaxial structure with identical growth conditions. The different layers are outlined by the background colors, from left to right: contact layer (CL), window (W), emitter, base, and collector.

S2: Supplementary band diagrams

Figure S2a depicts a band diagram under illumination and voltage bias of a 3T *npn* device in which it has been assumed that the majority carrier quasi-Fermi Level (MC-QFL) bends in the base layer, instead of the minority carrier (mC-)QFL. We have located that bending in the B-C space charge region (SCR) because we have assumed a high electrical doping in the base layer, as it is the case in our HBTSC prototype. Under high doping a MC-QFL bending in the neutral zone is ruled out because the layer is expected to remain under low injection, with the MC density, and hence the MC-QFL position, fixed by the electrical doping. Nevertheless, assuming instead that the doping level is moderate, and the bending takes place in the neutral zone, would not change our argument. The diagram shows that, in the case of MC-QFL bending, the voltage at the top junction $V^{top} = V_E - V_B$ equals the voltage at the bottom junction $V^{bot} = V_C - V_B$. We make then the following observations:

(i) If a bending takes place in a MC-QFL it must be necessarily small, because the hole current density, is given by $\boldsymbol{J}_h = p\,\mu_h\,\boldsymbol{\nabla} E_{F,h}$, where p is the hole concentration and μ_h is the hole mobility. The gradient operator in this equation is the mathematical representation of the "bending". Assuming a large gradient would imply an unrealistically large current given the large value of p. Therefore, if the MC-QFL bends, $V^{top} = V^{bot}$ are not expected to achieve values markedly higher than those produced in a homojunction made of the small band-gap material unless μ_h approaches zero. In the case of a mC-QFL bending, $\boldsymbol{J}_e = n\,\mu_e\,\boldsymbol{\nabla} E_{F,e}$ can be relatively small even for a large bending of $E_{F,e}$ because n is many orders of magnitude smaller than p, even if the doping is moderate.

(ii) Following the argument presented in the main text, the entropy production (σ_h) associated to the hole current is proportional to $\boldsymbol{J_h} \cdot \boldsymbol{\nabla} E_{F,h}$. The full expression is: [1]

$$\sigma_h = \frac{1}{e\,T}\,\boldsymbol{J}_h \cdot \boldsymbol{\nabla} E_{F,h}$$

where T is the temperature. As discussed, a MC-QFL bending would be characterized by a large J, and therefore, the power loss under operation (FF degradation) would be severe.

(iii) The HBTSC prototype exhibits experimentally $V_{OC}^{top} > V_{OC}^{bot}$, which is consistent with the band diagram depicted in Figure 2c in the main text (mC-QFL bending) and not with the one in Figure S2a here (MC-QFL bending). Following the point made in (ii), this means that the power loss (FF degradation) when the device is biased at a high V^{top} can be small.

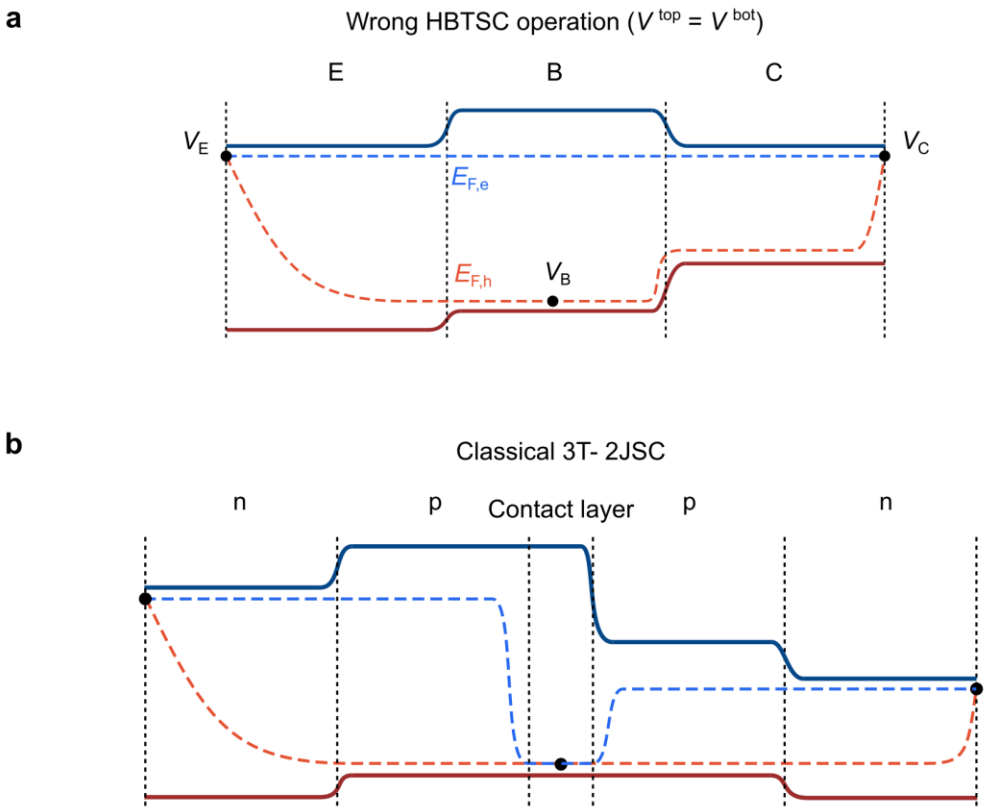

Figure S2: Device band diagrams under illumination and bias voltage. (a) npn structure which does not behave in agreement with the HBTSC model due to a flawed design or wrong choice of material parameters. (b) Classical 3T-2JSC where the two junctions are separated by a contact layer.

Figure S2b shows the band diagram under illumination and voltage bias of a classical three-terminal double-junction solar cell (3T-2JSC). This device is built by stacking, or depositing, two pn-junctions back to back. The operation of this device shows many similarities to the HBTSC, albeit with a less compact design. The main difficulties found in 3T-2JSCs which are absent in the HBTSC are the need to passivate the surfaces in contact with the contact layer to achieve high carrier selectivity (high V_{OC}) in both sub-cells, and the need to implement a contact layer which is highly-conductive and transparent.

S3: Device geometry and efficiency calculations

The device in Figure S3a is the HBTSC prototype with independent power extraction from the two junctions, characterized in Figures 2 and 3 in the main text. The device in Figure S3b is called test device in the main text, see Figure 5. Both have been fabricated following the same process on the same epitaxial structure.

The test device does not behave as an HBTSC (no independent power extraction) as a result of a resistive voltage drop across the base layer.

Table S1 compiles three definitions of area for the two junctions in each device:

(i) The junction areas. The bottom junction area (white dashed rectangles in Figure S3) is defined by the mesa etch and the top junction area (white dashed rectangles) is defined by the GaInP (emitter) etch. Junction area measurements have a relatively high uncertainty because of irregularities in the etch walls, especially the GaInP etch.

(ii) The illumination areas, obtained by subtracting the area covered by metal from the junction area.

(iii) The whole mesa area. In this case we apply the bottom junction area to both junctions.

Table S1 also contains the AM1.5G photoconversion efficiencies (η) calculated using the illumination, junction, and full mesa areas. The large discrepancy between the efficiencies calculated scaling by the illumination areas and the full mesa area is explained by the fact that in these proof-of-concept devices the emitter has been etched to deposit the base contact and the metal pads have not been minimized.

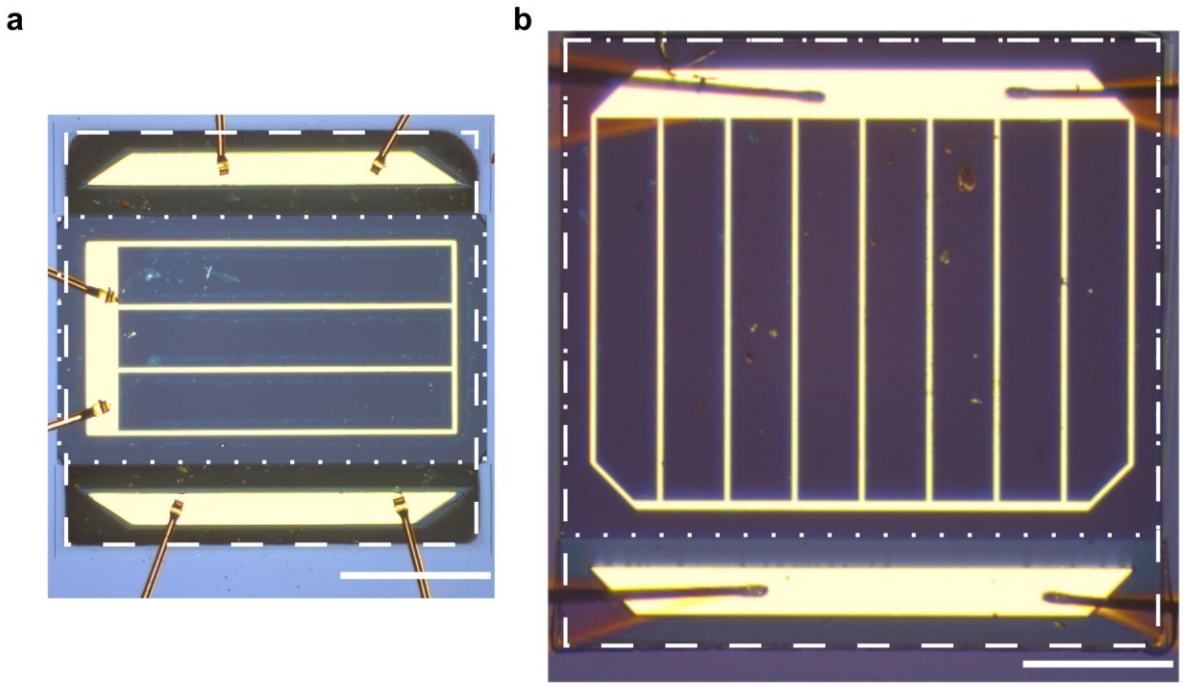

Figure S3: Micrographs of the two HBTSC devices discussed in the main text. (a), HBTSC prototype, (b) test device. In both cases, the area of the bottom (top) junction is highlighted by a white dashed square (dotted rectangle). Scalebars are 500 μm long.

Table S1: Area definitions and photoconversion efficiencies (η) calculated using different area definitions.

	HBTSC prototype			test device		
junction	top	bottom	total	top	bottom	total
illumination area [mm²]	1.03 ± 0.06	1.57 ± 0.11		2.84 ± 0.12	3.32 ± 0.12	
junction area [mm²]	1.16 ± 0.05	1.93 ± 0.10		3.28 ± 0.10	4.01 ± 0.09	
full mesa area [mm²]	1.93 ± 0.10	1.93 ± 0.10		4.01 ± 0.09	4.01 ± 0.09	
η calculated using illumination area [%]	15.9 ± 1.5	11.9 ± 1.3	27.8 ± 2.9	14.4 ± 1.2	10.4 ± 0.8	24.8 ± 2.0
η calculated using junction area [%]	14.0 ± 1.1	9.7 ± 0.9	23.7 ± 2.0	12.8 ± 0.9	8.5 ± 0.5	21.3 ± 1.4
η calculated using whole mesa area [%]	8.5 ± 0.8	9.7 ± 0.9	18.2 ± 1.6	10.5 ± 0.7	8.5 ± 0.5	19.0 ± 1.2

S4: Supplementary EQE data

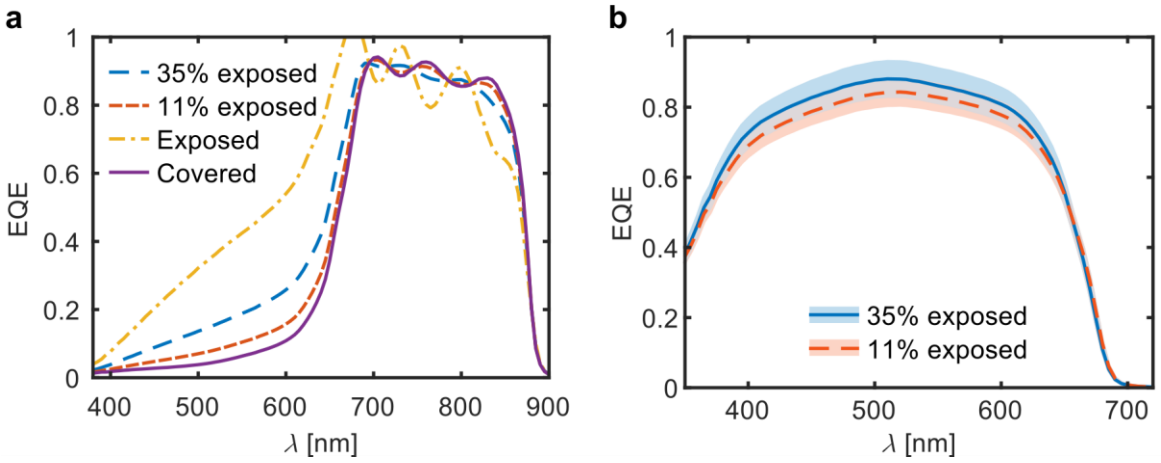

Figure S4.1: External quantum efficiency (EQE) measurements of the two devices depicted in Figure S3. (a) EQE of the bottom junctions. (b) EQE of the top junctions.

The HBTSC prototype has a region in which the emitter has been etched. To obtain the EQE that is representative of the intact HBTSC structure (Figure 2e in the main text), we have combined the measurements of the two device geometries. In the device in Figure S3a 35% of the bottom-junction area exposed (the emitter has been etched) and in the device in Figure S3b it is 11%. The corresponding EQE measurements are plotted in Figure S4a.

We call the measured EQEs of the two samples EQE_1 and EQE_2, and define the exposed (B_i) and covered (A_i) normalized area fractions, where *i* is either 1 or 2. Because the measured bottom junction EQEs result from two regions in parallel, one covered ($EQE_{covered}$) and the other exposed ($EQE_{exposed}$), we can write the following linear combination:

$$EQE_i = A_i\, EQE_{covered} + B_i\, EQE_{exposed}$$

The resulting curves are also plotted in Figure S4.1a. The $EQE_{covered}$ curve is the one shown in Figure 2e in the main text. Because it represents the intact HBTSC layer structure, it is fitted with the theoretical model to analyze the contribution of the base absorption to the photocurrent of either junction. As expected, this curve is lower than the measured curves in the spectral range where the emitter absorbs. Note that the oscillations caused by optical resonance are a non-linear effect and, therefore, they cannot be reproduced with precision using this method.

Figure S4.1b shows the EQE of the top junctions of both devices. The shadowed areas represent the uncertainty resulting from measuring the illumination areas. Both EQEs are in good agreement within the measurement error, which implies that resistive effects related to the different device geometries do not have a significant impact on the EQE and supports the use of a linear combination to eliminate the problem of the exposed area in the bottom junction EQE.

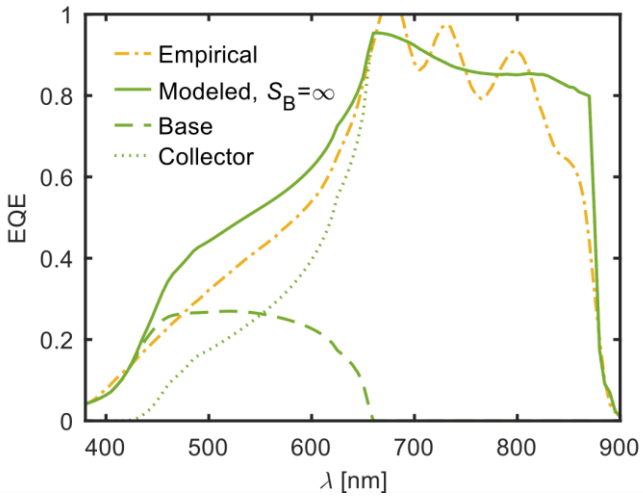

Figure S4.2: External quantum efficiency (EQE) for a fully exposed bottom junction obtained from experimental data compared to the theoretical modelling. All parameters used for this modelling are the same used for Figure 2e and compiled in Table 2 in the main text (modelling of a fully covered bottom junction) except for the ones affected by the etch. The contributions of the base and collector layers to the modelled EQE are also shown.

Now we quantify the effect of the emitter etch on the measured bottom-junction photocurrent (J_{SC}^{bot}). In the device regions where the emitter has been etched, the light reaching the bottom junction is unfiltered by the top junction. This leads to an overestimation of the photocurrent, but the extent of this overestimation is limited by the large surface recombination velocity (S_B) of the base front surface that is exposed in the etching. To prove this, Figure S4.2 shows again the empirical EQE extrapolated for a hypothetical fully exposed bottom junction (yellow dash-dotted line) and compares it to a modelled EQE curve (green solid line). The modelled curve results from solving the continuity equations for minority carriers in each layer as we did for Figure 2e in the main text, but this time we remove the emitter layer, assume a 430 nm thickness for the base layer (~200 nm were removed from the base layer to isolate the base contact) and set $S_B = \infty$. All other parameters, such as mobilities and diffusion lengths, are kept the same. It is observed that the condition of very high S_B can reproduce the empirical EQE of the exposed regions in the short-wavelength range.

Table S2 compiles the J_{SC}^{bot} values obtained by integrating the four EQE curves shown in Figure S4 over the AM1.5G spectrum. From those values it is inferred that in our HBTSC prototype the contribution of exposed regions leads to an increase of 13% in J_{SC}^{bot} with respect to a hypothetical non-etched structure.

Table S2: Bottom junction current densities under AM1.5G illumination calculated from the integration of empirical EQEs.

	HBTSC prototype (35% exposed)	Test device (11% exposed)	Hypothetical fully covered	Hypothetical fully exposed
J_{SC}^{bot} [mA cm^{-2}]	15.9 ± 1.1	14.7 ± 0.5	14.0 ± 2.1	19.5 ± 8.7

S5: Modelling of optical absorption

Figure 2e in the main text shows the measured and modeled EQE of the HBTSC prototype before depositing the ARC. Figure S5 shows the same measurement and compares it to the calculated absorptance of each layer (colored areas). Note that, for simplicity, we have added the base absorptance to the bottom junction EQE, although the EQE modeling shows that it contributes to both junctions.

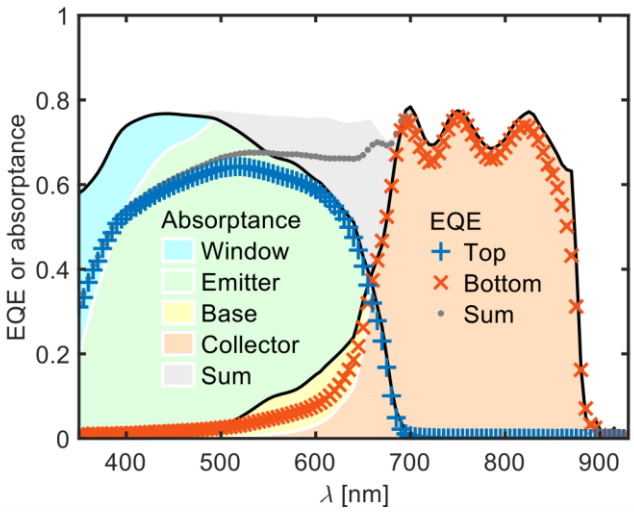

Figure S5: EQEs of the HBTSC prototype before depositing the ARC, together with the calculated absorptance of each layer (colored areas). Experimental EQE values are marked by crosses.

S6: Supplementary characterization of luminescent coupling

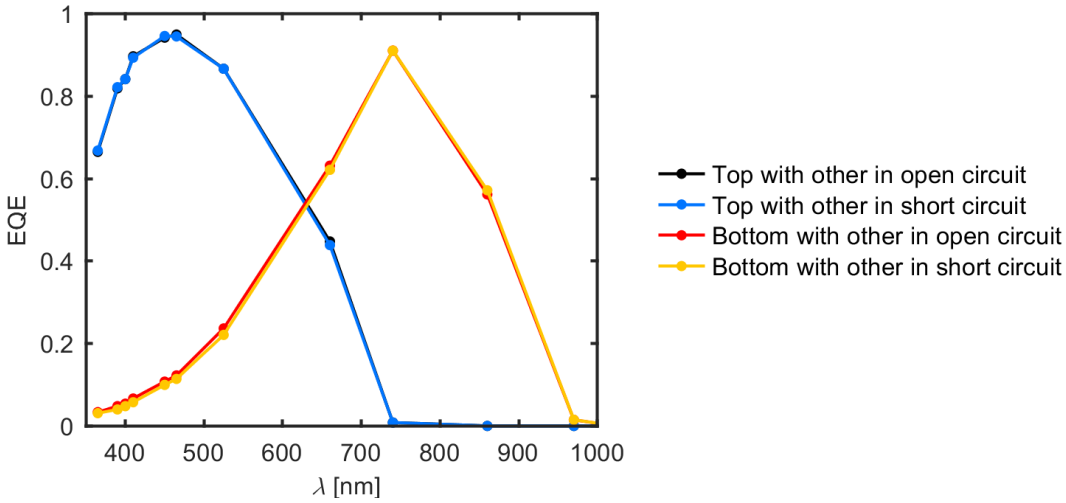

Figure S6: Alternative measurement of the absolute EQE of the HTBSC prototype, performed with the LED solar simulator by powering one wavelength at a time. The slight difference in the 390-660 nm range between the bottom junction EQEs measured when the top junction was in OC and when the top junction was in SC is consistent with the existence of photon coupling, which is also perceived in the J-V curves. This difference was not observable in the EQE measurements taken with the monochromator because the low light intensity produces a low voltage bias of the top cell. Note that carrier injection from the top junction into the bottom junction cannot explain this extra photocurrent because an equivalent bias of the top junction under dark conditions does not affect the current measured through the bottom junction.

S7: Dark *J-V* curves

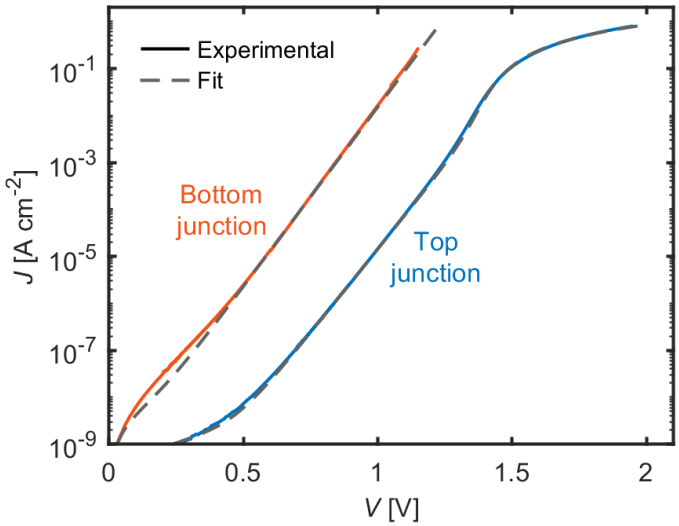

Figure S7: Dark J-V curves for top junction (blue solid line) and bottom junction (red solid line), and the fits to a two-exponential model (grey dashed lines) including series and parallel resistance components. The parameters for the fits are given in the main text Table 1. The dark curves are not affected by the bias of the not-measured junction (for voltages $\lessapprox$ the corresponding one-sun V_{OC}).

S8: SIMS profile of compensated contact

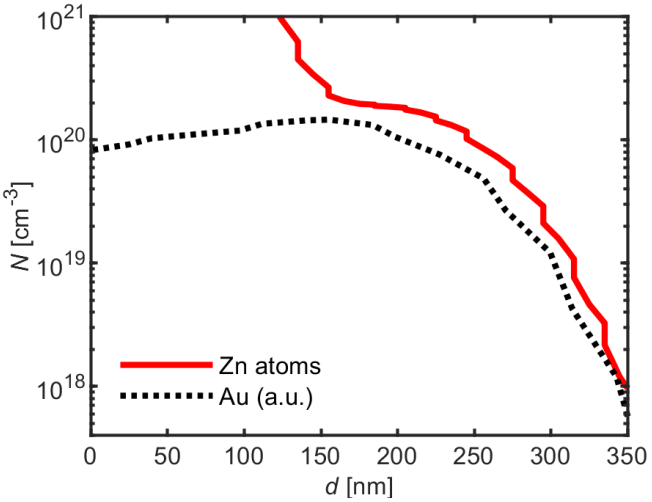

Figure S8: SIMS measurement of compensated contact. Doping atom concentration (N) as function of distance from semiconductor-metal interface (d) measured by SIMS on an epitaxial structure grown with the same conditions as our HBTSC prototype. The base contact (15 nm Au / 40 nm Zn / 500 nm Au) was evaporated on top of the 25 nm thick window layer and the 350 nm thick emitter. The contact was annealed for 180 s at 420 °C. A Zn concentration greater or equal to the base epitaxial Zn concentration is found down to a depth of 250 nm.

S9: Series resistance model

The method to calculate the series resistance has been taken from Luque[2] and adapted to our geometry. In this method, a lumped resistance is obtained for each element of the structure from the calculation of the power loss produced in that element. The current path throughout the HBTSC device and the resistance components can be seen in Figure S9.

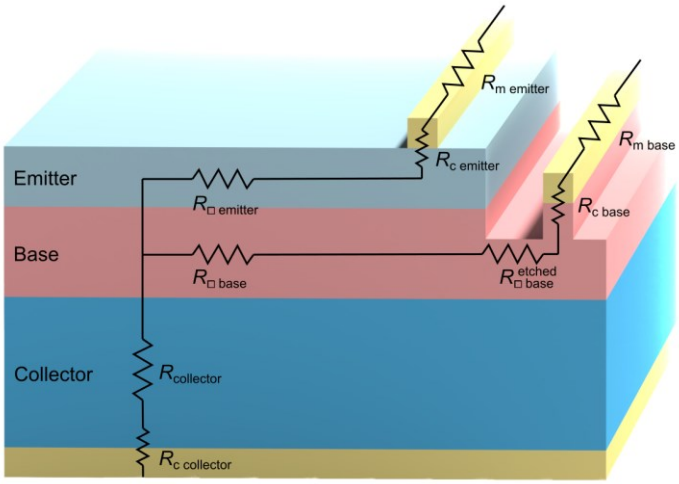

Figure S9: Series resistance model: current path throughout the solar cell. Charge carriers encounter different components of series resistance before leaving the solar cell.

The resistance of the collector ($R_{collector}$), as well as the contact resistances ($R_{c\ (emitter,\ collector,\ base)}$) are calculated straightforward. For the contributions of emitter, base and metal fingers, the model accounts for the fact that current is photogenerated uniformly all over the layer and photogenerated current accumulates along the transport lines. Departing from the majority carrier mobilities [3–5] (μ_i), the doping level (N_i) (SIMS measurement, assuming complete ionization) and the elementary charge (q) we calculate the resistivity (ρ_i) of each layer i:

$$\rho_i = (N_i * \mu_i * q)^{-1}$$

Taking into account the thickness (w_i), we get the sheet resistance ($R_{\square\,i}$):

$$R_{\square\,i} = \rho_i\, w_i^{-1}$$

The resistance $r_{s\,i}$ of a layer of length l_i with crowding due to lateral current flow is then[2]:

$$r_{s\,i} = \frac{1}{3}\, R_{\square\,i}\, l_i^2$$

This formula can be applied directly to calculate the resistance of the emitter, $R_{s\ emitter}$, and its metallization grid, $R_{m\ emitter}$. For the lateral contribution of the base we must take into account that there is an etched region where the base is thinner (the trench that isolates the base contact, with length l_{etch}). The contribution to the top junction resistance arising from the lateral transport in the base is then:

$$R^{top}_{s\ base} = \frac{1}{3}\, R_{\square\ base}\, l_e^2 + R^{etched}_{\square\ base}\ l_{etch} l_e$$

where we have neglected the collection of photocurrent from the trench.

In the case of the bottom junction, where current is also generated in the trench, we calculate the series resistance by a weighted average of the sheet resistance in etched and unetched areas:

$$R^{bot}_{s\ base} = \frac{1}{3}\, \frac{R_{\square base}\, l_e\ +\ R^{etched}_{\square base}\ l_{etch}}{l_e\ +\ \ l_{etch}}\ l_b^2$$

In Table S3, we compare the modeled with the experimental voltage drops ΔV produced by J_{SC} of one junction in the *J-V* curves of the other junction.

Table S3: Voltage drops at V_{OC} observed in J-V curves of one junction when changing the bias of the other junction from open circuit to short circuit.

	HBTSC prototype		test device	
	top	bottom	top	bottom
ΔV_{OC} experimental	9	6	74	51
ΔV_{OC} modeled	9	5	78	64

S10: Voltage maps of the test device

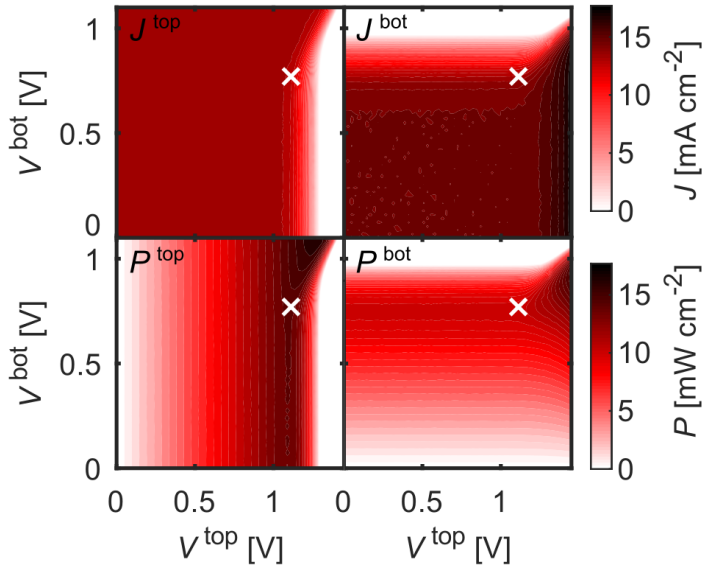

Figure S10: J-V-V maps of the test device under AM1.5G illumination. Maps on the left correspond to the top junction, on the right to the bottom junction. Upper plots show current density and lower plots show power density.

S11: 2T HBTSC-on-Si architecture

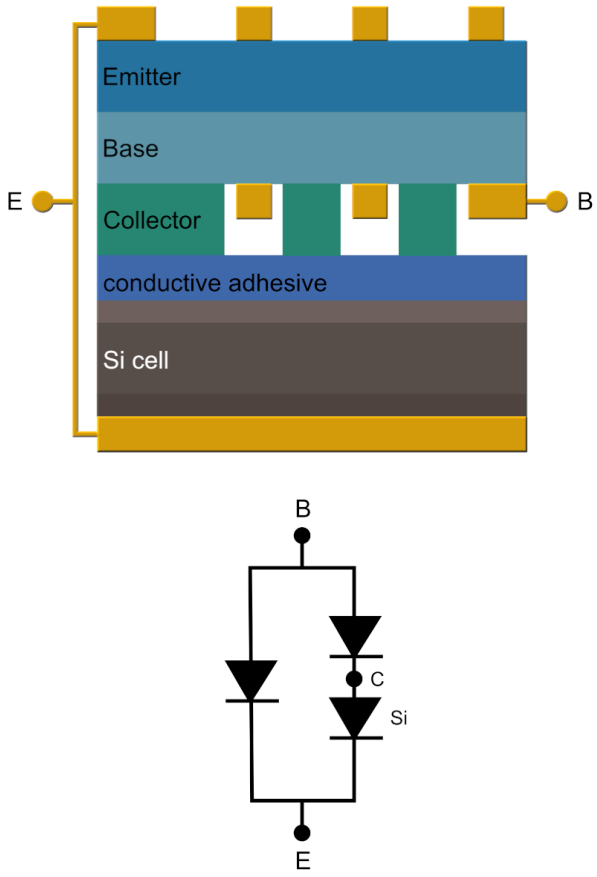

Figure S11: Schematic and equivalent circuit of a 2T-3JSC made of an HBTSC and a silicon cell as proposed in Antolín et al.[6] . The transparent conductive adhesive connects the collector of the HBTSC to the top contact of the Si cell. The detailed balance efficiency under AM1.5G illumination of architecture using a lattice-matched GaInP/GaAs HBTSC is 43% [6].

S12: Top interdigitated and bottom interdigitated base contact

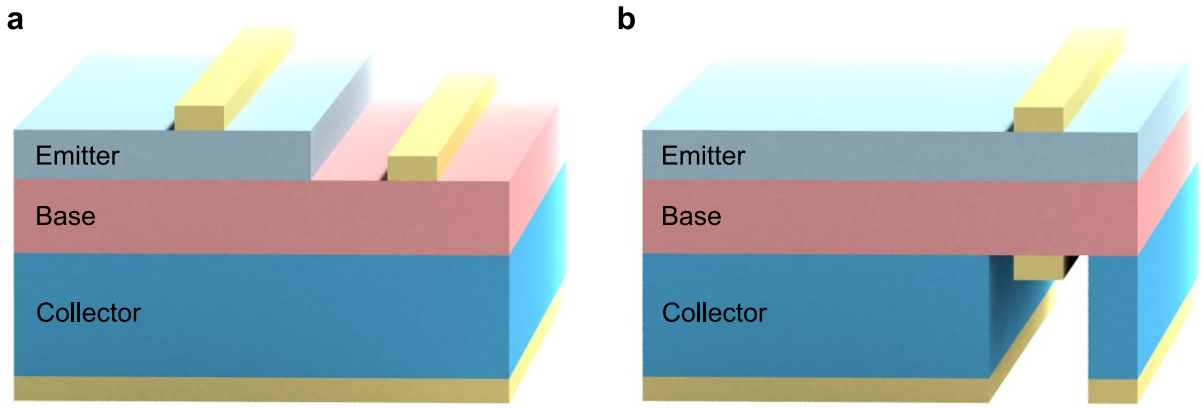

Figure S12: Contact strategies for the base contact. a, top interdigitated base contact. The base contact is made through the top surface, removing part of the top junction and introducing additional shadow besides the emitter contact. b, bottom interdigitated base contact. The base contact is made through the bottom surface, removing part of the bottom junction. For this contact strategy, the substrate most likely needs to be removed.

SUPPLEMENTARY REFERENCES

1. Luque, A., and Martí, A. (2011). Theoretical Limits of Photovoltaic Conversion and New-Generation Solar Cells. In Handbook of Photovoltaic Science and Engineering (Chap. 4, Eds. A. Luque and S. Hegedus, John Wiley & Sons, Chichester), pp. 130–168, doi:10.1002/9780470974704.ch4.

2. Luque, A., and Araújo, G.L. (1989). Solar cells and optics for photovoltaic concentration (A. Hilger).

3. Shitara, T., and Eberl, K. (1994). Electronic properties of InGaP grown by solid-source molecular-beam epitaxy with a GaP decomposition source. Appl. Phys. Lett. *65*, 356–358, doi:10.1063/1.112373.

4. Ikeda, M., and Kaneko, K. (1989). Selenium and zinc doping in $Ga_{0.5}In_{0.5}P$ and $(Al_{0.5}Ga_{0.5})_{0.5}In_{0.5}P$ grown by metalorganic chemical vapor deposition. J. Appl. Phys. *66*, 5285–5289, doi:10.1063/1.343718.

5. Sotoodeh, M., Khalid, A.H., and Rezazadeh, A.A. (2000). Empirical low-field mobility model for III–V compounds applicable in device simulation codes. J. Appl. Phys. *87*, 2890–2900, doi:10.1063/1.372274.

6. Antolín, E., Zehender, M.H., Svatek, S.A., García-Linares, P., and Martí, A. (2020). III-V-on-silicon triple-junction based on the heterojunction bipolar transistor solar cell concept. In 2020 47th IEEE Photovoltaic Specialists Conference (PVSC), pp. 1226–1231, doi:10.1109/PVSC45281.2020.9300681.